Journal of Materials Chemistry A

Synthesis and Photocatalytic Properties of Metastable β-Bi2O3 Stabilized by Surface-Coordination Effects

Journal:	*Journal of Materials Chemistry A*
Manuscript ID:	TA-ART-11-2014-006235.R1
Article Type:	Paper
Date Submitted by the Author:	07-Jan-2015

Complete List of Authors:	Jiang, Haiying; National Institute for Materials Science, Research Unit for Enviromental Remediation Materials; Renmin University of China, Department of Chemistry Li, Peng; National Institute for Materials Science, Liu, Guigao; National Insititute for Materials Science, Research Unit for Enviromental Remediation Materials Science Ye, Jinhua; National Institute for Materials Science, Lin, Jun; Renmin University of China, Chemistry Department

Cite this: DOI: 10.1039/c0xx00000x

www.rsc.org/xxxxxx

ARTICLE TYPE

Synthesis and Photocatalytic Properties of Metastable β-Bi_2O_3 Stabilized by Surface-Coordination Effects

Hai-Ying Jiang[a, b], Peng Li[a], Guigao liu[a], Jinhua Ye*[a, c], and Jun Lin*[b]

Received (in XXX, XXX) Xth XXXXXXXXX 20XX, Accepted Xth XXXXXXXXX 20XX

DOI: 10.1039/b000000x

Metastable semiconductor, β-Bi_2O_3, was successfully synthesized with the precursor of $Bi_2O_2CO_3$ in this study, which showed much higher photocatalytic activity in the photooxidation of isopropyl alcohol (IPA) than thermal stable α-Bi_2O_3. The prepared samples were characterized by X-ray diffraction (XRD), field emission scanning electron microscope (FE-SEM), and high-resolution transmission electron microscope (HRTEM). Based on the previous study, a surface CO_3^{2-} coordination effect was proposed to understand the formation mechanism of β-Bi_2O_3 at room temperature. This speculation was supported by the surface chemical states' differences between α- and β-Bi_2O_3, which were studied by Fourier transform infrared spectroscope (FT-IR), X-ray photoelectron spectroscope (XPS) and thermogravimetric-differential thermal analysis (TG-DTA). Meanwhile, the energy band structures of α- and β-Bi_2O_3 were measured with ultraviolet-visible diffuse reflection spectrascope (UV-vis DRS) and valence band X-ray photoelectron spectroscope (VB-XPS); the electronic structures were calculated using the plane-wave density functional theory (DFT) with the CASTEP program package. At last, the photo-induced charge separation efficiency and photocarriers' lifetime of α-Bi_2O_3 and β-Bi_2O_3 were studied by steady state and dynamic photoluminescence (PL). Based on the results, the higher photocatalytic activity of β-Bi_2O_3 than that of α-Bi_2O_3 was attributed to its higher visible light harvest, the formation of $O_2^{-\cdot}$ with strong oxide ability, higher charge separation efficiency, and larger surface areas.

1. INTRODUCTION

In the past decades, semiconductor photocatalysis attracted increasing attentions as a potential green technology to solve environmental pollution and energy shortage[1]. TiO_2, as the most known photocatalysts[2], has been extensively studied in the applications of the environmental cleaning and energy conversion due to its unique properties, such as chemical inertness, strong oxide ability, long-term stability against photo & chemical corrosion, cost effectiveness, and nontoxic[2]. However, the relatively wide band gap (3.2 eV) limits its photo-absorption to the only UV-light, hindering its practical applications in our daily life[3]. As a result, a serious of narrow band-gap semiconductors (≤ 3.0 eV) have been developed to realize the efficient utilization of visible light, which accounts for about 40 % of the total sunlight[4-6]. Bi_2O_3 crystals have been demonstrated to be a family of potential photocatalysts due to their appropriate band gaps[7].

Bi_2O_3 has six polymorphic forms, monoclinic α- phase , tetragonal β- phase, body-centered cubic γ- phase, face-centered cubic δ- phase, tetragonal ε- phase, and triclinic ω- phase. Among them, α- phase is the most stable phase at room temperature; δ- phase is the stable phase at high temperature (730 ^oC - 825 ^oC); the other four phases, i. e. β, γ, ε, and ω- phase, are metastable phase[8]. It was found that photocatalysts with different crystal structures show quite different photocatalytic performances[9]. The previous study shows that α-Bi_2O_3, β-Bi_2O_3 and δ-Bi_2O_3 exhibit good photocatalytic activities in the degradation of pollutants[7]. Up to now, α-Bi_2O_3 was mostly studied because of its thermal stability and easy preparation[10-13]. However, the most active polymorph was proved to be β-Bi_2O_3[7, 14-16]. Since it is a metastable phase, much less research was reported. In the recent literatures, β-Bi_2O_3 was successfully prepared by using $Bi_2O_2CO_3$ as a precursor[7]. Nevertheless, the formation mechanism is still unclear, and it's difficult to controllably stabilize this metastable phase at room temperature. Therefore, it is important and meaningful to address this issue through a detailed research on the formation mechanism of β-Bi_2O_3 at room temperature.

In this study, α-Bi_2O_3 and β-Bi_2O_3 were selectively synthesized with the same precursor of $Bi_2O_2CO_3$ under different calcination temperatures. The prepared samples were characterized by X-ray diffractometer (XRD), field-emission electron microscope (FE-SEM) and high-resolution transmission electron microscope (HRTEM). The energy band structures of the samples were studied by the UV-visible diffuse reflectance spectroscopy (UV-vis DRS), valence band X-ray photoelectron spectroscopy (VB-XPS), combined with the theoretical calculations. The photocatalytic properties were studied by the oxidation of IPA over α-Bi_2O_3 and

β-Bi_2O_3 under visible light irradiations. The formation mechanism of β-Bi_2O_3 at room temperature was studied by the surface chemical states' differences of α-Bi_2O_3 and β-Bi_2O_3, using Fourier transform infrared (FT-IR) spectrophotometer, X-ray photoelectron spectroscope (XPS) and thermogravimetric-differential thermal analysis (TG-DTA). At last, the photo-induced charge separation efficiency and photocarriers' lifetime of α-Bi_2O_3 and β-Bi_2O_3 were studied by steady state and dynamic photoluminescence (PL), which are important and meaningful for explaining the higher photocatalytic activity of β-Bi_2O_3 than α-Bi_2O_3 in the photooxidation of isopropyl alcohol (IPA).

2. EXPERIMENTAL SECTION

2.1 Material Preparation.

α-Bi_2O_3 and β-Bi_2O_3 were synthesized with $Bi_2O_2CO_3$ as the precursor. A typical preparation procedure of $Bi_2O_2CO_3$ was as follows[17]: Firstly, 5.21g of Bi $(NO_3)_3 \cdot 5 H_2O$ was dissolved in 27 mL of dilute HNO_3 (1 M), while 6.78 g of Na_2CO_3 was dissolved in 107 mL of ultrapure water; Secondly, the Na_2CO_3 solution was added into the Bi $(NO_3)_3$ solution dropwise under constant stirring. At this step, large amounts of white precipitate was formed; Next, the suspension was stirred for 15 minutes, and further maintained at 60 °C for 12 hours without stirring; Finally, the product was collected and washed with ultrapure water and ethanol several times before being dried at 60 °C for 6 hours. Here, $Bi_2O_2CO_3$ was successfully prepared. In order to get α-Bi_2O_3 and β-Bi_2O_3, the prepared $Bi_2O_2CO_3$ was heated to 400 °C and 350 °C respectively with a rate of 10 °C·min^{-1}, and remained for 30 minutes.

2.2 Sample Characterizations.

The crystal structures of the precursor and Bi_2O_3 samples were determined with an X-ray diffractometer (X'pert Powder, PANalytical B. V., Netherlands) with Cu - Kα radiation. Field-emission electron microscope (FE-SEM) was performed to observe the morphologies on a JEOL 6701F microscope. High-resolution transmission electron microscope images were recorded with a high-resolution transmission electron microscope (HRTEM, Tecnai G2F30). The diffuse reflection spectra were measured with an integrating sphere equipped ultraviolet-visible (UV-vis) recording spectrophotometer (UV-2500PC, Shimadzu Co., Japan) using $BaSO_4$ as reference and the optical absorption spectra were converted from the diffuse reflection spectra according to the Kubelka-Munk equation. The specific surface areas were determined with a surface analyzer (BEL Sorp-mini II, BEL Japan Co., Japan) through nitrogen adsorption and desorption isotherms at 77K by the Brunauer-Emmett-Teller (BET) method. The FT-IR spectra were obtained with a Fourier transform-infrared (FT-IR) spectrophotometer (IRPrestige-21, Shimadzu Co., Japan). X-ray photoelectron spectroscopy (XPS) was performed on an ESCALAB 250Xi spectrometer equipped with 300W Al Kα radiation, while all binding energies were referenced to the C1s peak (284.6 eV) of the surface adventitious carbon. Thermogravimetric-differential thermal analysis (TG-DTA; Shimadzu, DTG-60H, Japan) was used to study the details in the calcination process of $Bi_2O_2CO_3$ at different temperatures. Steady state and dynamic PL of samples were measured using an excitation wavelength of 325 nm diode laser, respectively, on a Fluorolog-3 spectrofluorometer (Horiba Jobin Yvon). The experiments were carried out under ambient conditions.

2.3 Photocatalytic oxidations of IPA.

The photocatalytic oxidations of gaseous IPA were carried out to evaluate the photocatalytic activities of Bi_2O_3 samples. The experiments were carried out under visible light irradiation (420nm ≤ λ ≤ 800nm). The light source was a 300 W Xe-arc lamp (10 A imported current, focused through a 50 × 50 mm^2 shutter window) equipped with wavelength cut-off filters and a water filter. 100 mg of Bi_2O_3 powder was bespread uniformly on a glass dish with an area of 9 cm^2. A certain amount of gaseous IPA (~ 1400 ppm) was injected into the vessel and kept for 2 hour in the dark before irradiations. During the irradiation by visible light, 0.5 ml of the gas was sampled everyone 1 hour intervals. The products were analyzed with a gas chromatograph (GC-2014, Shimadzu, Japan) with a flame ionization detector (FID). Furthermore, the adsorption of IPA in dark over α-Bi_2O_3 and β-Bi_2O_3 were also carried out without light irradiation, as well as the self-degradation of IPA under visible light irradiation (420nm ≤ λ ≤ 800nm) without any catalyst.

2.4 Theoretical Calculation.

The band structures of α- and β-Bi_2O_3 were calculated using the plane-wave density functional theory (DFT) with the CASTEP program package. The core electrons were replaced by ultrasoft pseudopotentials with a plane-wave basis cutoff energy of 380.0 eV, and the interactions of exchange and correlation were treated within the framework of the local density approximation (LDA). The FFT grids of basis in all the models were 40 × 54 × 48 and 54 × 54 × 40 for α-Bi_2O_3 and β-Bi_2O_3, respectively. The k-point sets of 3 × 2 × 2 for α - Bi_2O_3 and 2 × 2 × 2 for β-Bi_2O_3 were used.

3. RESULTS AND DISCUSSIONS

3.1 Crystal structures.

The crystallographic phases of the prepared Bi_2O_3 and precursor samples were characterized by X-ray diffraction (XRD). As described in Fig. 1, the precursor shows a good single orthorhombic crystal phase of $Bi_2O_2CO_3$, and all the peaks are accordance with the standard database (ICSD No. 70-8631)[18]. When the precursor was calcined for 30 minutes at 350 °C, the crystal changed to β-Bi_2O_3 in tetragonal crystal corresponding to the ICSD file of No. 27-0050[19]. With an increase of the calcination temperature to 400 °C, the crystal gradually changed to α-Bi_2O_3

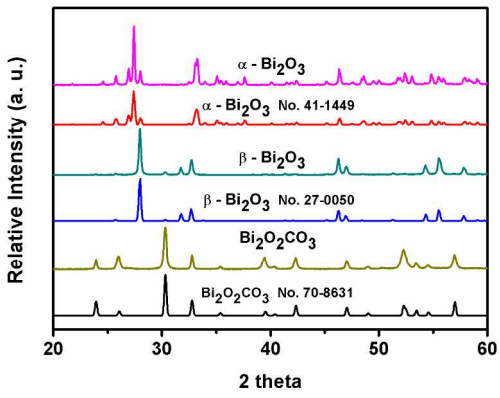

Fig. 1 XRD patterns of $Bi_2O_2CO_3$, α-Bi_2O_3 and β-Bi_2O_3

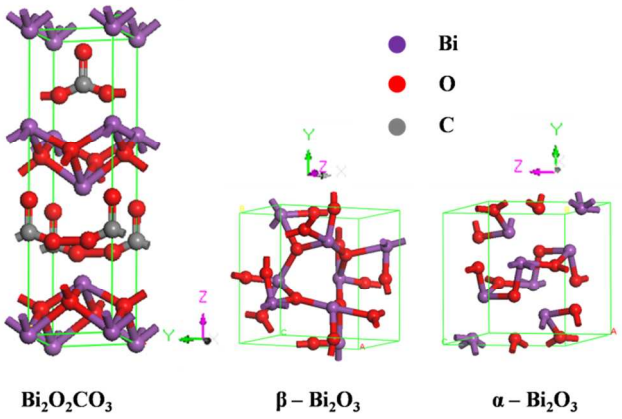

Fig. 2 Schematic crystal structures of $Bi_2O_2CO_3$, α-Bi_2O_3 and β-Bi_2O_3

after 30 minutes. All the diffraction peaks could approximately be indexed to a monoclinic α-Bi_2O_3 (ICSD No. 41-1449)[19]. The schematic crystal structures of $Bi_2O_2CO_3$, β-Bi_2O_3 and α-Bi_2O_3[18, 19] were displayed in Fig. 2. Therefore, α-Bi_2O_3 and β-Bi_2O_3 can be selectively prepared by $Bi_2O_2CO_3$ at different calcination temperatures.

The crystal structures of the precursor and Bi_2O_3 samples were further confirmed by field-emission scanning electron microscopy (FE-SEM) and high-resolution transmission electron microscopy. From Fig. 3, we can see that $Bi_2O_2CO_3$ precursor is constituted by large amounts of nanosheets [Fig. 3 (A)]; β-Bi_2O_3 sample is composed of the nanosheets and smaller nanoparticles [Fig. 3 (B)]; α-Bi_2O_3 sample mainly consists of the nanoparticles with the size of about 300 nm [Fig. 3 (C)]. The morphology changes of the samples probably results from the decomposition of $Bi_2O_2CO_3$ precursor[20]. As exhibited in Fig. 3 (D), two sets of orthorhombic fringes with the lattice spacing of 0.293 nm and 0.278 nm could be indexed to the (103) and (110) planes of orthorhombic $Bi_2O_2CO_3$. Fig. 3 (E) shows that the lattice space is measured to be 0.295 nm, matching with the space of the (211) crystal plane of tetragonal β-Bi_2O_3. From Fig. 3 (F), the lattice with a space of 0.332 nm is observed, which is corresponded to the (111) planes of monoclinic α-Bi_2O_3. In addition, the BET surface areas of α-Bi_2O_3 and β-Bi_2O_3 were measured to be 3.6 and 4.5 m^2/g, respectively.

3.2 Energy band structures.

The UV-vis absorption spectra of α-Bi_2O_3 and β-Bi_2O_3 samples are

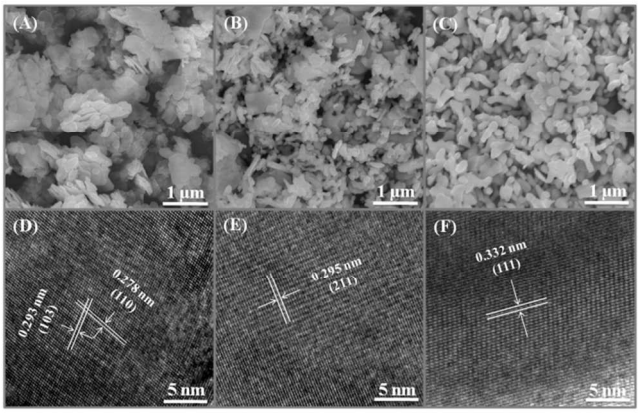

Fig. 3 SEM and HRTEM of $Bi_2O_2CO_3$ [(A) and (D)], α-Bi_2O_3 [(B) and (E)] and β-Bi_2O_3 [(C) and (F)].

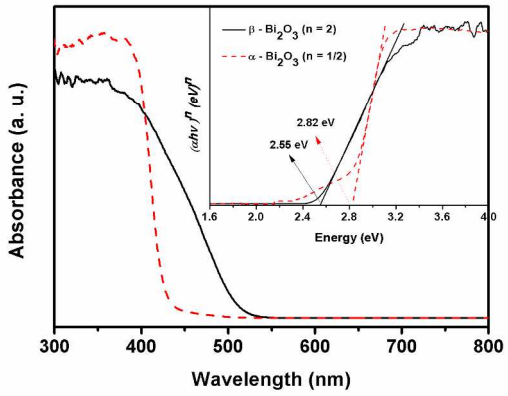

Fig. 4 UV-vis absorption spectra of the as-prepared α-Bi_2O_3 and β-Bi_2O_3; The inset is the corresponding Tauc Plots curves.

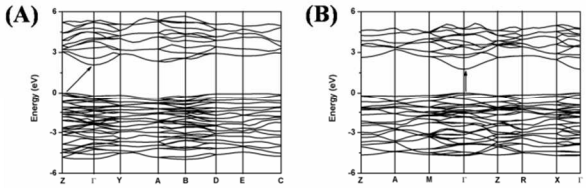

Fig. 5 Calculated band structures of α-Bi_2O_3 (A) and β-Bi_2O_3 (B).

displayed in Fig. 4, and both of the samples show high visible light responses. The absorption edges of α-Bi_2O_3 and β-Bi_2O_3 are about 430 nm and 520 nm, respectively. The band gaps (E_g) of α-Bi_2O_3 and β-Bi_2O_3 are determined by the following equation[21] (Tauc equation):

$$(\alpha hv)^n = A\,(hv - E_g)$$

In this equation, α, v, A and E_g are the absorption coefficient, light frequency, proportionality constant, and band gap. The value of the index n depends on the property of the materials: for the direct band-gap semiconductors, n = 2; for the indirect band-gap semiconductors, n = 1/2[22]. According to the electronic structures calculation of α-Bi_2O_3 and β-Bi_2O_3, α-Bi_2O_3 is an indirect semiconductor [Fig. 5 (A)], and β-Bi_2O_3 is a direct semiconductor [Fig. 5 (B)]. Therefore, the value of n is determined to be 1/2 for α-Bi_2O_3, while it is 2 for β-Bi_2O_3. Based on the results, we can get the Tauc plots of $(\alpha hv)^n$ *vs.* photo energy, as shown in the inset of Fig. 4. The band gaps of α-Bi_2O_3 and β-Bi_2O_3 are estimated from the tangent lines to be 2.82 eV and 2.55 eV, respectively. The calculated band gaps of α-Bi_2O_3 and β-Bi_2O_3 in Fig. 5 are 2.08 eV and 1.76 eV, which are smaller than the experimental value. This difference may be caused by the limitation of the LDA functional that underestimates the band gaps in semiconductor simulation. Both the experimental and theoretical results show that β-Bi_2O_3 possesses a narrower band gap than α-Bi_2O_3, and the narrower band gap indicates a higher visible light absorption.

Furthermore, VB-XPS were also carried out to study the energy band structures of α-Bi_2O_3 and β-Bi_2O_3. As shown in Fig. 6, the energy differences between the Fermi levels and the valence bands of α-Bi_2O_3 and β-Bi_2O_3 are almost the same, and the value is + 1.35 eV. According to the earlier literatures, the Fermi levels of α-Bi_2O_3 and β-Bi_2O_3 are + 1.73 eV[23] and + 0.54 eV[24], respectively. Combining the energy differences between the Fermi levels and the valence bands, the value of the Fermi levels, and the band gaps of α-Bi_2O_3 and β-Bi_2O_3, we can get their detailed energy band

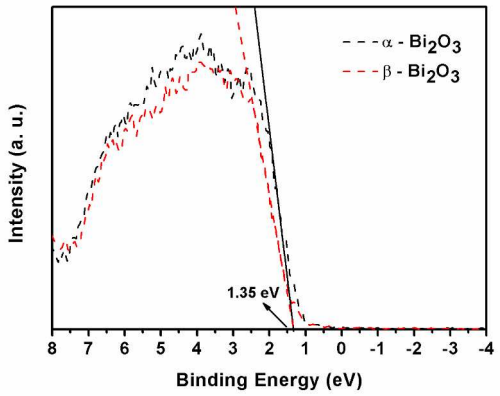

Fig. 6 VB-XPS spectra of α-Bi_2O_3 and β-Bi_2O_3

Table 1 Energy band structures of α-Bi_2O_3 and β-Bi_2O_3

	Band Gap (eV)	Valence Band (eV vs. NHE)	Conduction Band (eV vs. NHE)	Fermi Level (eV vs. NHE)
α - Bi_2O_3	2.82	+3.08	+0.26	+1.73
β - Bi_2O_3	2.55	+1.89	-0.66	+0.54

structures, as shown in Table 1.

3.3 Effect of CO_3^{2-} on the stability of β-Bi_2O_3.

To understand the formation mechanism of β-Bi_2O_3, FT-IR and XPS measurements were used to study the surface conditions of α-Bi_2O_3 and β-Bi_2O_3.

For the FT-IR spectra [Fig. 7 (A)] of β-Bi_2O_3, the intensive peaks at about 850 cm^{-1} and 1395 cm^{-1} can be attributed to the v_2 and v_3 mode of CO_3^{2-}. These vibration peaks of CO_3^{2-} are possibly generated from the residual carbonate on the surface of β-Bi_2O_3 [350 °C, Fig. 7 (B)]. All the peaks derived from CO_3^{2-} have sharply decreases in the IR spectra with the increase of the calcination temperatures, and the XRD pattern in Fig. 7 (B) shows that the prepared samples calcined at 400 °C, 450 °C, and 500 °C, are monoclinic α-Bi_2O_3. In addition, the intensity decrease of the peaks derived from CO_3^{2-} means that CO_3^{2-} contents on the surface of Bi_2O_3 decreases as the calcination temperature increases[25].

To get more detailed information of the surface chemical states and compositions of the elements in the prepared α-Bi_2O_3 and β-Bi_2O_3, XPS analysis were carried out. From Fig. 8 (A), the presence of Bi, O and C were revealed in the survey spectra of α-Bi_2O_3 and β-Bi_2O_3. Then firstly, two types of carbon were found in Fig. 8 (B), and they are attributed to the surface adventitious carbon and the carbon in CO_3^{2-} group[25, 26]. The percentage of carbon for CO_3^{2-} in β-Bi_2O_3 is determined to be 29 %, while it is a little less in α-Bi_2O_3 (26 %). Next, from Fig. 8 (C), the two characteristic peaks of Bi^{3+} in both α-Bi_2O_3 and β-Bi_2O_3 were observed and ascribed as $Bi4f_{5/2}$ and $Bi4f_{7/2}$[27]. We can also see that the two peaks of β-Bi_2O_3 with slightly higher energy than those of α-Bi_2O_3. This is probably because of more CO_3^{2-} exists on the surface of β-Bi_2O_3. At last, the XPS peaks of O1s were displayed in Fig. 8 (D). According to the earlier literatures, the three peaks were attributed to the oxygen in H - O - H[28], CO_3^{2-} [29]and Bi - O - Bi[27]. Similarly to Fig. 8 (B), the oxygen for CO_3^{2-} in β-Bi_2O_3 (52 %) is also more than that in α-Bi_2O_3 (44 %).

Therefore, the XPS results also prove that the CO_3^{2-} on the surface of β-Bi_2O_3 is more than that of α-Bi_2O_3, which is the same

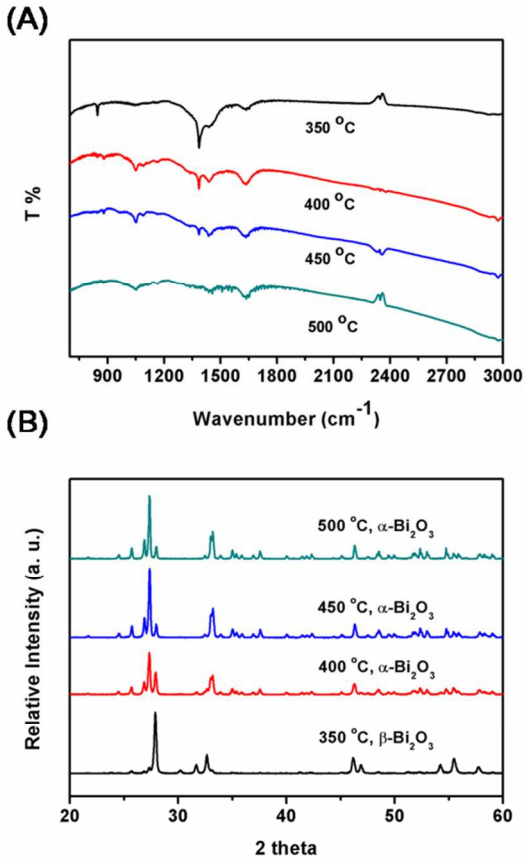

Fig. 7 FT-IR (A) and XRD (B) spectra of the samples decomposed by $Bi_2O_2CO_3$ precursor at different temperatures.

with the FT-IR results.

It is known that, β-Bi_2O_3 is only stable at about 650 °C, and it will transform to α-Bi_2O_3 when it is cooled down to room temperature[8]. However, as mentioned previously, β-Bi_2O_3 can often be successfully prepared by heating $Bi_2O_2CO_3$ at low temperature and stable at room temperature. We can't help to ask, what factors make it stable at room temperature. In the earlier literatures[9], the surface-coordinated organic ligands were proved to be effective to lower the surface energy of $NaNbO_3$ and induce the formation of cubic $NaNbO_3$, which is also a metastable phase. Based on this explanation, the similar speculation is proposed in this paper. $Bi_2O_2CO_3$ crystal can be gradually decomposed when it is heated to the temperature of that higher than 308 °C. In this process, the carbonate ions in its crystal structures will move out from the interior to the surface, and then leave the body of the $Bi_2O_2CO_3$ crystals, releasing CO_2. When the temperature is not high enough (350 °C), there will be some CO_3^{2-} left on the surface of Bi_2O_3 crystals, inducing the formation of the metastable β-Bi_2O_3; However, when the calcination temperature was increased to higher temperature (400 °C or above), less CO_3^{2-} will be left on the surface of β-Bi_2O_3 crystals after 30 minutes. In this case, the left surface-coordinated CO_3^{2-} is not enough to keep the crystal structure of β-Bi_2O_3, inducing the crystal structure transformation to thermal stable α-Bi_2O_3 (As shown in Scheme 1). In other words, the surface-coordinated CO_3^{2-} can lower the surface energy of β-Bi_2O_3, and make it stable at room temperature. In addition, the speculation was further studied by TG-DTA to confirm this decomposition detail of the $Bi_2O_2CO_3$ precursor in the calcination process. From the TGA spectra in Fig. 9, about 8 % weight losses are both observed in the two different calcination processes

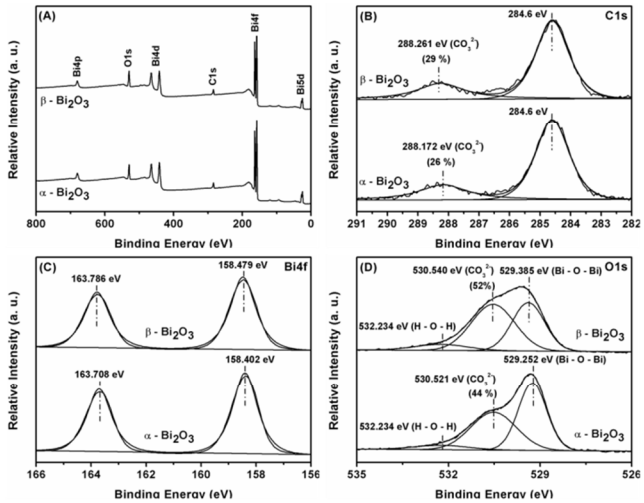

Fig. 8 XPS spectra of (A) survey; (B) C1s; (C) Bi4f; (D) O1s for α-Bi_2O_3 and β-Bi_2O_3.

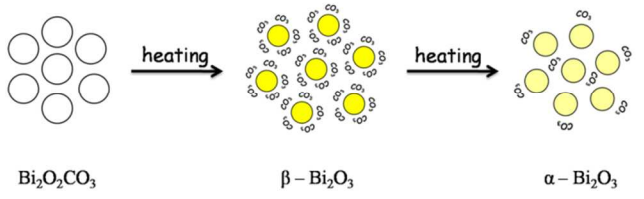

Scheme 1 Schematic diagram of the decomposition process to form β-Bi_2O_3 and α-Bi_2O_3.

(350 °C and 400 °C for 30 min), corresponding to the theoretical weight loss (8.6 %) due to the removal of CO_2. We also observe that the weight loss at 400 °C for 30 min is slightly more than that at 350 °C for 30 min, which indicates that more CO_3^{2-} was removed for forming α-Bi_2O_3. As the DTA curves, accompanied with the weight loss processes of the TGA curves, there are a thermonegative peak and a thermopositive peak during the formation process of α-Bi_2O_3, while there are only one thermonegative peak during the formation process of β-Bi_2O_3. The common thermonegative peak (peak 1) of the two processes is attributed to the decomposition of $Bi_2O_2CO_3$ and the formation of β-Bi_2O_3, and the thermopositive peak (peak 2) in the formation process of α-Bi_2O_3 is due to the transformation from β-Bi_2O_3 to α-Bi_2O_3[20]. Therefore, the TG-DTA results well explain the detailed decomposition process of $Bi_2O_2CO_3$ to β-Bi_2O_3 and α-Bi_2O_3 at different calcination temperatures.

3.4 Photocatalytic oxidation of IPA.

The photocatalytic activities of both α-Bi_2O_3 and β-Bi_2O_3 were evaluated by the oxidation of gaseous IPA under visible light irradiation. In the IPA oxidation, the production of acetone, the unique observed product, was as the main index to judge the reaction activities. After 8 hours' irradiation by visible light ($420nm \leq \lambda \leq 800nm$), the acetone productions over α-Bi_2O_3 and β-Bi_2O_3 samples were determined to be 1045 ppm and 485 ppm, respectively, while the negligible acetone was produced from IPA under visible light irradiation in the absence of any catalyst [Fig. 10]. Obviously, β-Bi_2O_3 shows higher photocatalytic activity in the oxidation of IPA than α-Bi_2O_3. Meanwhile, the adsorption of IPA by α-Bi_2O_3 and β-Bi_2O_3 samples in the dark was also carried out.

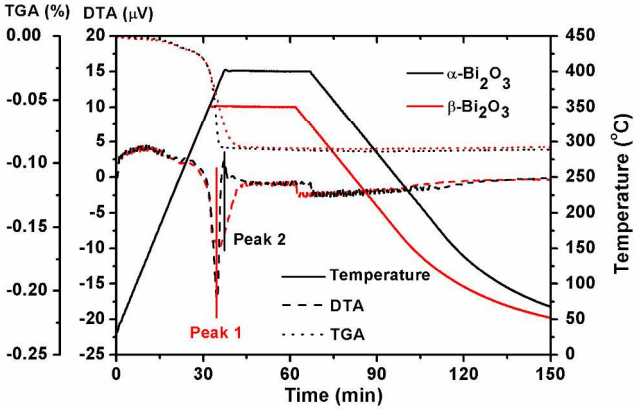

Fig. 9 TG-DTA of the $Bi_2O_2CO_3$ calcined at 350 °C and 400 °C for 30 min.

The results show that the acetone production was negligible under these conditions. The difference in the photocatalytic activity between α-Bi_2O_3 and β-Bi_2O_3 is probably attributed to their different band gaps. Since β-Bi_2O_3 has a narrower band gap than α-Bi_2O_3, it can absorb more visible light in a wider region, implying higher photocatalytic activity under visible light irradiation.

It was reported that, IPA can be photocatalytic oxidized through two typical reaction processes as below[30]:

(1) h^+ oxidation:

$$CH_3CHOHCH_3 + h^+ \rightarrow CH_3COCH_3 + 2H^+ + e^-$$

(2) O_2 oxidation:

$$CH_3CHOHCH_3 + e^- + O_2 + H^+ \rightarrow CH_3COCH_3 + HO\cdot + H_2O$$

Between them, since $O_2^{-\cdot}$ will be produced in the O_2 oxidation process[31, 32], α-Bi_2O_3 can only oxide the IPA molecular to acetone through h^+ oxidation process, due to its low conduction band (+ 0.26 V *vs.* NHE). Meanwhile, β-Bi_2O_3 can realize the IPA oxidation to acetone through both the two processes because of its higher conduction band potential (- 0.66 V *vs.* NHE) than the oxide reaction of O_2 to $O_2^{-\cdot}$ (- 0.33 V *vs.* NHE). This is another important reason of that β-Bi_2O_3 shows much higher photocatalytic activity than α-Bi_2O_3. The differences of the photocatalytic oxidation mechanism of the IPA to acetone by α-Bi_2O_3 and β-Bi_2O_3 are described detailedly in Scheme 2.

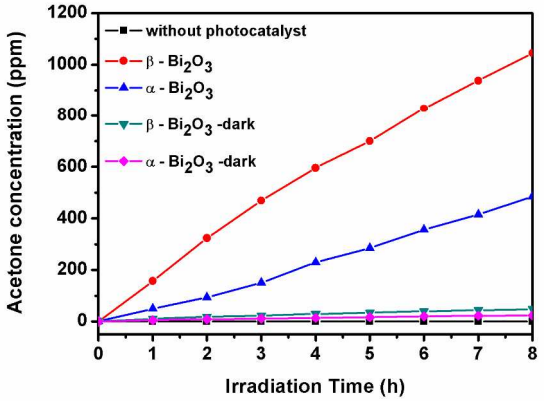

Fig. 10 Photocatalytic oxidation of gaseous IPA over α-Bi_2O_3 and β-Bi_2O_3 under different conditions.

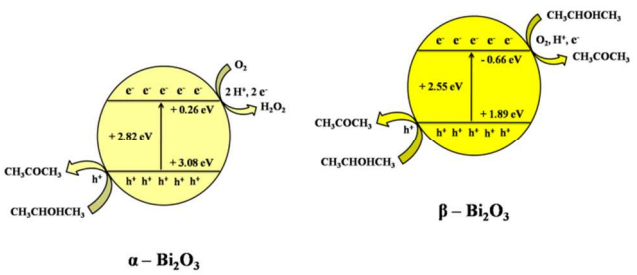

Scheme 2 Photocatalytic oxidation of gaseous IPA over α-Bi_2O_3 and β-Bi_2O_3 under different conditions.

At last, the photo-induced charge separation efficiency and photocarriers' lifetime of α-Bi_2O_3 and β-Bi_2O_3 were studied by steady state and dynamic photoluminescence [Fig. 11 (A) and (B)]. It is clearly observed in Fig. 11 (A) that both α-Bi_2O_3 and β-Bi_2O_3 exhibits significant emission peaks, which are related to the photocarriers' recombination of them. In these spectra, the PL intensity of β-Bi_2O_3 is much lower than that of α-Bi_2O_3, which indicates that β-Bi_2O_3 shows higher photo-induced charge separation efficiency than α-Bi_2O_3. In addition, the photocarriers' lifetime of β-Bi_2O_3 is also slightly longer than that of α-Bi_2O_3, by comparing their decay time of the photocarriers. These results also support that the photocatalytic activity of β-Bi_2O_3 is higher than that of α-Bi_2O_3 to some extent.

Besides, lager surface area of β-Bi_2O_3 (4.5 m^2/g) than that of α-Bi_2O_3 (3.6 m^2/g) is also an important reason of its higher photocatalytic activity.

Based on the results and analysis above, the higher photocatalytic activity of β-Bi_2O_3 than α-Bi_2O_3 is attributed to the following four reasons: (1) the narrower band gap of β-Bi_2O_3 than that of α-Bi_2O_3 indicates higher visible light harvest; (2) higher conduction band potential of β-Bi_2O_3 than that of α-Bi_2O_3 results in the formation of $O_2^{-\cdot}$ with strong oxide ability; (3) higher charge separation efficiency; (4) larger surface area of β-Bi_2O_3 than that of α-Bi_2O_3. These four factors collectively explain the higher photocatalytic activity of β-Bi_2O_3 in the IPA oxide reaction.

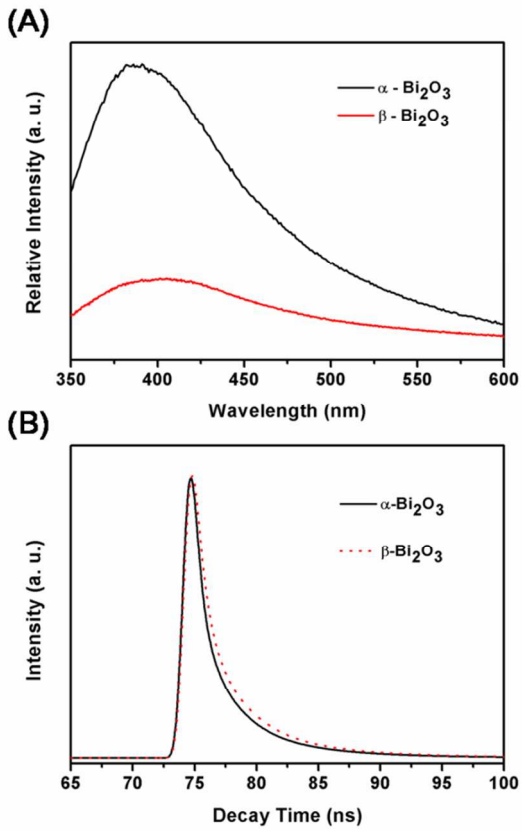

Fig. 11 Steady state (A) and dynamic photoluminescence (B) over α-Bi_2O_3 and β-Bi_2O_3.

4. CONCLUSIONS

In conclusion, α-Bi_2O_3 and β-Bi_2O_3 were selectively synthesized with the same precursor of $Bi_2O_2CO_3$ under different calcination temperatures. The formation mechanism of β-Bi_2O_3 was studied by analyzing the surface chemical states of α-Bi_2O_3 and β-Bi_2O_3 through FT-IR and XPS spectra. The results indicate that the surface-coordinated CO_3^{2-} can lower the surface energy of β-Bi_2O_3 and make it stable at room temperature. The photocatalytic performances of α-Bi_2O_3 and β-Bi_2O_3 for the oxidation of IPA were also studied in this work; β-Bi_2O_3 shows much higher photocatalytic activity than α-Bi_2O_3, which is attributed to its higher visible light harvest, the formation of $O_2^{-\cdot}$ with strong oxide ability, higher charge separation efficiency and larger surface areas. The study on the formation mechanism of β-Bi_2O_3 provides the important guidance for its preparations. This work also proves that the surface chemical states of the materials have significant effects on their crystal structures' stabilities, further affecting their photocatalytic activities.

ACKNOWLEDGEMENT

This work was partially supported by the World Premier International Research Center Initiative (WPI Initiative) on Materials Nanoarchitectonics (MANA), MEXT, Japan, the National Natural Science Foundation of China (21273281), the National Basic Research Program of China (973Program, No. 2013CB632405 and No. 2014CB239301), the Fundamental Research Funds for the Central Universities and the Research Funds of Renmin University of China (13XNH121), and the National Scholarship Fund.

Notes and references

[a] *Research Unit for Environmental Remediation Materials, National Institute for Materials Science (NIMS), 1-1, Namiki, Tsukuba, Ibaraki 305-0044, Japan. Fax: +81-29-860-4958; Tel: +81-29-859-2646; E-amil: Jinhua.YE@nims.go.jp*

[b] *Department of Chemistry, Renmin University of China, Beijing 100872, People's Republic of China. Fax:+86-10-62516444; Tel: +86-10-62514133; E-mail: jlin@chem.ruc.edu.cn*

[c] *TU-NIMS Joint Research Center, School of Material Science and Engineering, Tianjin University, 92 Weijin Road, Tianjin, P.R. China*

1. H. Tong, S. Ouyang, Y. Bi, N. Umezawa, M. Oshikiri and J. Ye, *Adv. Mater.*, 2012, **24**, 229-251.
2. M. R. Hoffmann, S. T. Martin, W. Choi and D. W. Bahnemann, *Chem. Rev.*, 1995, **95**, 69-96.
3. A. Tanaka, S. Sakaguchi, K. Hashimoto and H. Kominami, *ACS Catal.*, 2012, **3**, 79-85.
4. C. Zhang and Y. Zhu, *Chem. Mater.*, 2005, **17**, 3537-3545.
5. C. Santato, M. Odziemkowski, M. Ulmann and J. Augustynski, *J. Am. Chem. Soc.*, 2001, **123**, 10639-10649.

6. A. Kudo, K. Omori and H. Kato, *J. Am. Chem. Soc.*, 1999, **121**, 11459-11467.
7. H. Cheng, B. Huang, J. Lu, Z. Wang, B. Xu, X. Qin, X. Zhang and Y. Dai, *Phys. Chem. Chem. Phys.*, 2010, **12**, 15468-15475.
8. M. Drache, P. Roussel and J.-P. Wignacourt, *Chem. Rev.*, 2007, **107**, 80-96.
9. P. Li, S. Ouyang, Y. Zhang, T. Kako and J. Ye, *J. Mater. Chem. A*, 2013, **1**, 1185-1191.
10. H.-Y. Jiang, K. Cheng and J. Lin, *Physical Chemistry Chemical Physics*, 2012, **14**, 12114-12121.
11. A. Hameed, T. Montini, V. Gombac and P. Fornasiero, *J. Am. Chem. Soc.*, 2008, **130**, 9658-9659.
12. Z. Bian, J. Zhu, S. Wang, Y. Cao, X. Qian and H. Li, *J. Phys. Chem. C*, 2008, **112**, 6258-6262.
13. H.-Y. Jiang, J. Liu, K. Cheng, W. Sun and J. Lin, *J. Phys. Chem. C*, 2013, **117**, 20029-20036.
14. L. Yin, J. Niu, Z. Shen and J. Chen, *Environ. Sci. Technol.*, 2010, **44**, 5581-5586.
15. X. Xiao, R. Hu, C. Liu, C. Xing, C. Qian, X. Zuo, J. Nan and L. Wang, *Appl. Catal. B-Environ.*, 2013, **140**, 433-443.
16. M. Schlesinger, S. Schulze, M. Hietschold and M. Mehring, *Dalton Trans.*, 2013, **42**, 1047-1056.
17. H. Cheng, B. Huang, K. Yang, Z. Wang, X. Qin, X. Zhang and Y. Dai, *Chem. Phys. Chem*, 2010, **11**, 2167-2173.
18. J. D. Grice, *Can. Mineral.*, 2002, **40**, 693-698.
19. H. A. Harwig, *Z. Anorg. Allg. Chem.*, 1978, **444**, 151-166.
20. Z. Ai, Y. Huang, S. Lee and L. Zhang, *J. Alloys Compd.*, 2011, **509**, 2044-2049.
21. P. Li, S. Ouyang, G. Xi, T. Kako and J. Ye, *J. Phys. Chem. C*, 2012, **116**, 7621-7628.
22. M. A. Butler, *J. Appl. Phys.*, 1977, **48**, 1914-1920.
23. C. Li, J. Zhang and K. Liu, *Int. J. Electrochem. Sci.,*, 2012, **7**, 5028-5034.
24. H. Fan, H. Li, B. Liu, Y. Lu, T. Xie and D. Wang, *ACS Appl. Mater. Interfaces*, 2012, **4**, 4853-4857.
25. H. Lu, L. Xu, B. Wei, M. Zhang, H. Gao and W. Sun, *Appl. Sur. Sci.*, 2014, **303**, 360-366.
26. P. Madhusudan, J. Yu, W. Wang, B. Cheng and G. Liu, *Dalton Trans.*, 2012, **41**, 14345-14353.
27. H.-Y. Jiang, G. Liu, M. Li, J. Liu, W. Sun, J. Ye and J. Lin, *Appl. Catal. B-Environ.*, 2015, **163**, 267-276.
28. A. Makarowicz, C. L. Bailey, N. Weiher, E. Kemnitz, S. L. M. Schroeder, S. Mukhopadhyay, A. Wander, B. G. Searle and N. M. Harrison, *Phys. Chem. Chem. Phys.*, 2009, **11**, 5664-5673.
29. H. Xu, Y. Song, Y. Song, J. Zhu, T. Zhu, Chengbao Liu, D. Zhao, Q. Zhang and H. Li, *RSC Adv.*, 2014, **4**, 34539-34547.
30. S. Ouyang and J. Ye, *J. Am. Chem. Soc.*, 2011, **133**, 7757-7763.
31. F. Arsac, D. Bianchi, J. M. Chovelon, C. Ferronato and J. M. Herrmann, *J. Phys. Chem. A*, 2006, **110**, 4202-4212.
32. Y. Ohko, K. Hashimoto and A. Fujishima, *J. Phys. Chem. A*, 1997, **101**, 8057-8062.

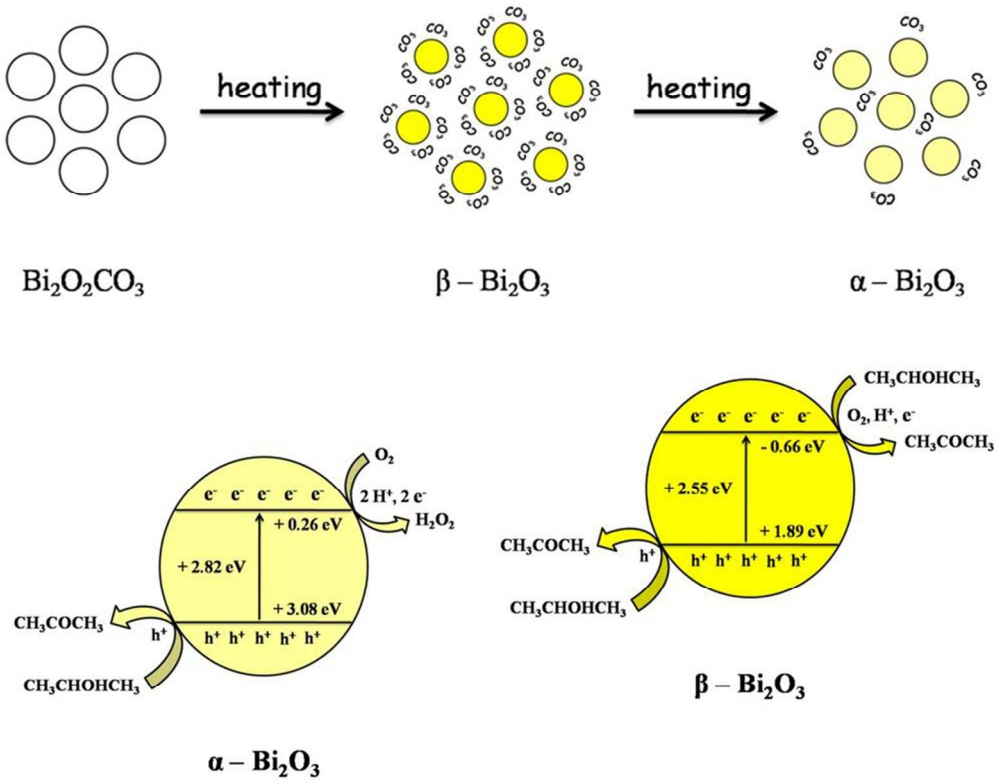

169x133mm (150 x 150 DPI)